Fast simulation of 3D electromagnetic problems using potentials

E. Haber* U. M. Ascher† D.A. Aruliah‡
D. Oldenburg§

May 7, 2000

Abstract

We consider solving three-dimensional electromagnetic problems in parameter regimes where the quasi-static approximation applies, the permeability is constant, the conductivity may vary significantly, and the range of frequencies is moderate. The difficulties encountered include handling solution discontinuities across interfaces and accelerating convergence of traditional iterative methods for the solution of the linear systems of algebraic equations that arise when discretizing Maxwell's equations in the frequency domain.

We use a potential-current formulation $(\boldsymbol{A}, \phi, \widehat{\boldsymbol{J}})$ with a Coulomb gauge. The potentials $\boldsymbol{A}$ and ϕ decompose the electric field $\boldsymbol{E}$ into components in the active and null spaces of the $\nabla \times$ operator. We develop a finite volume discretization on a staggered grid that naturally employs harmonic averages for the conductivity at cell faces. After discretization, we eliminate the current and the resulting large, sparse, linear system of equations has a block structure that is diagonally dominant, allowing efficient solution with preconditioned Krylov

*Department of Computer Science and Institute of Applied Mathematics, University of British Columbia, Vancouver, BC, V6T 1Z4, Canada. (`haber@cs.ubc.ca`).

†Department of Computer Science, University of British Columbia, Vancouver, BC, V6T 1Z4, Canada. (`ascher@cs.ubc.ca`).

‡Department of Computer Science and Institute of Applied Mathematics, University of British Columbia, Vancouver, BC, V6T 1Z4, Canada. (`dhavide@cs.ubc.ca`).

§Department of Earth and Ocean Science, University of British Columbia, Vancouver, BC, V6T 1Z4, Canada. (`doug@geop.ubc.ca`).

space methods. A particularly efficient algorithm results from the combination of BICGSTAB and an incomplete LU-decomposition. We demonstrate the efficacy of our method in several numerical experiments.

Keywords: vector potential, Helmholtz decomposition, Coulomb gauge, Maxwell's equations, solution discontinuities, finite volume, Krylov space methods, preconditioning.

1 Introduction

Fast, accurate solutions of 3-D electromagnetic equations are required to simulate responses from geophysical surveys and also for solving the electromagnetic inverse problem. Difficulties arise when attempting to find corresponding three-dimensional numerical solutions. These difficulties include handling regions of (almost) vanishing conductivity, handling different resolutions in different parts of the spatial domain, handling the multiple scale lengths over which the physical properties can vary, and handling regions of highly varying conductivity, magnetic permeability or electrical permittivity where jumps in solution properties across cell interfaces may occur.

We consider Maxwell's equations in the frequency domain over a frequency range which excludes high frequencies (in a sense to be made more precise following (1) below). The permeability is assumed constant. The piecewise smooth conductivity structure σ partitions the spatial domain into disjoint subdomains and thus, normal components of the electric field may be discontinuous across interfaces between distinct materials. We consider a domain involving both ground and air [25, 12, 22]. This particular model is used in geophysical surveys where artificial or natural sources induce currents in conducting bodies.

A major obstacle in modeling such phenomena is that the conductivity in the air essentially vanishes. From an analytic perspective, the specific subset of Maxwell's equations used typically forms an almost-singular system in regions of almost-vanishing conductivity. Even in the ground (where the conductivity is not close to vanishing), the resulting differential operator is strongly coupled and not strongly elliptic [7]. Finding effective methods for solving the algebraic equations arising from careful, conservative discretizations of Maxwell's equations (as in [25, 18, 29]) has proved elusive in practice.

In [1], we addressed this concern by employing a Helmholtz decomposition first, using a potential formulation with a Coulomb gauge to obtain a system of strongly elliptic, weakly coupled differential equations. This change of variables (used in [4, 12, 21, 24] among others) splits the electric field into components in the active and null spaces of the $\nabla\times$ operator. Using a vertex-based discretization on a simple non-staggered grid, the resulting large, sparse algebraic systems were solved using preconditioned Krylov space methods [27, 2]. Combining BICGSTAB and a preconditioner comprising an incomplete LU-decomposition of the dominant system blocks resulted in a particularly efficient algorithm.

The discretization method in [1] is sufficiently accurate if σ is continuous or contains jumps that are small in magnitude. In the more general case which allows for a significantly discontinuous conductivity profile, it is difficult to devise an accurate discretization that preserves the benefits of the rapid solution techniques for the linear equations. This leads us to introduce the current density into the equations as an ultimately intermediate variable; the new analytic system is then discretized using a finite-volume technique on a staggered grid. The method is akin to mixed-hybrid finite element methods [33, 6, 23].

A staggered discretization for Maxwell's equations (originally proposed by Yee [35, 29]) has been considered in contexts similar to ours in [25, 22].[1] In this discretization, the Cartesian components of the electric field $\boldsymbol{E}$ and the magnetic field $\boldsymbol{H}$ are represented at distinct locations on the spatial grid (cf. [5]). Given a rectangular, three-dimensional grid, the components of $\boldsymbol{E}$ prescribed in [25, 22] are parallel to the edges of the cells and the components of $\boldsymbol{H}$ are orthogonal to the centers of the faces of the cells. This avoids the need to doubly define the (discontinuous) components of $\boldsymbol{E}$ in the normal directions to cell faces because the components of $\boldsymbol{E}$ used in this representation are tangential to the faces of the cells. However, when using a potential formulation to speed up the iterative solution of the algebraic equations, this placement of the field values becomes cumbersome. The complication is further increased if permeability is allowed to vary.

Thus, we develop a finite-volume method on a staggered grid using vector potentials, scalar potentials and generalized current densities as dependent variables. In Section 2, we develop the corresponding system of partial dif-

[1] We call it the Yee discretization, or method, even though Yee originally proposed his method for the time domain problem.

ferential equations (PDEs). This system is amenable to discretization using a finite-volume technique described in Section 3. For this discretization, the values of the components of the vector fields are associated with the centers of the faces of the cells and values of the scalar potential are associated with cell centers. The resulting scheme naturally employs harmonic averages for the conductivity σ on cell faces; it closely relates to a careful, efficient extension of the traditional Yee's method and retains various conservation properties for the fields.

We briefly describe the application of Krylov space methods to solve the system of algebraic equations in Section 4, complementing the description and numerical tests in [1]. Related methods were considered in [10, 11]. We use incomplete LU-decomposition, a powerful preconditioner in the case of diagonally dominant linear systems. The system's diagonal dominance is a direct consequence of our analytic formulation.

Finally, we present the results of numerical experiments in Section 5. We construct a synthetic example in 3D and demonstrate the accuracy of the method, even with large jump discontinuities in conductivity and even with coarse grids. We also demonstrate the rather significant efficiency gain of our method by comparing it to a method closer to the traditional Yee discretization using similar preconditioned Krylov space methods but without the potential reformulation [25]. As a rough general indication, our experimental MATLAB code requires about two minutes on a SPARC 10 workstation to solve the problem on a 32^3 grid. We also test the code on a geophysical problem and compare our results with those from another code.

We emphasize our view that the problem reformulation, the derivation of a suitable discretization scheme and the design of a fast iterative solver are all parts of one design process. Thus, the Helmholtz decomposition followed by a careful discretization allows for the construction of a simpler preconditioner for a standard Lanczos-type iteration. Others have chosen to discretize (1) (or the corresponding time-domain equations) first, and then manipulate the discrete equations [5, 3, 9], possibly with the view of designing a fast solver [17]. In the present setting our modular approach yields a complete scheme for fast 3D simulation which is easy to understand and implement by scientists and engineers.

2 Formulating the Electromagnetic Problem

With a time-dependence $e^{-i\omega t}$, Maxwell's equations in the frequency domain are

$$\nabla\times\ \boldsymbol{E} - \imath\omega\mu\boldsymbol{H} = \boldsymbol{0}, \tag{1a}$$
$$\nabla\times\ \boldsymbol{H} - (\sigma - \imath\omega\epsilon)\boldsymbol{E} = \boldsymbol{J^s}, \tag{1b}$$
$$\nabla\cdot\ (\epsilon\boldsymbol{E}) = \rho, \tag{1c}$$
$$\nabla\cdot\ (\mu\boldsymbol{H}) = 0, \tag{1d}$$

where μ is the magnetic permeability, ϵ is the electrical permittivity, $\boldsymbol{J^s}$ is a known source current density, and ρ is the (unknown) volume density of free charges. In our present work, we assume that $\mu > 0$ is constant and known. The physical properties $\epsilon > 0$ and $\sigma \geq 0$ can vary with position and are assumed bounded and piecewise smooth. We restrict the frequency range under consideration so that $\mu\epsilon\omega^2 L^2 \ll 1$, where L is a typical length scale. The electric field $\boldsymbol{E}$ and the magnetic field $\boldsymbol{H}$ are the unknowns in the forward modeling equations (1a,b), with the charge density ρ defined by (1c).

The system (1) is defined over an unbounded domain. However, in practice, we assume that (1) holds in a bounded subdomain $\Omega \subset \mathbb{R}^3$, and some combination of Dirichlet and Neumann boundary conditions (BCs) is imposed on the boundary $\partial\Omega$ of Ω. It is well-known that the existence of a unique, piecewise smooth solution $\boldsymbol{E}$ is guaranteed for a sufficiently smooth source and a wide variety of such BCs [20, 30, 5]. We thus assume that $\boldsymbol{E}$ has bounded second derivatives everywhere except in directions normal to material interfaces, and return to the choice of BCs towards the end of this section and in Section 5.

Often in the literature, (1a) is divided by μ, the $\nabla\times$ operator is applied, and (1b) is substituted into the resulting expression to obtain a second-order system of PDEs for the electric field $\boldsymbol{E}$, namely

$$\nabla\times\ (\mu^{-1}\nabla\times\ \boldsymbol{E}) - \imath\omega\widehat{\sigma}\boldsymbol{E} = \imath\omega\boldsymbol{J^s}, \tag{2}$$

where

$$\widehat{\sigma} := \sigma - \imath\omega\epsilon.$$

However, for reasons indicated in Section 1, we decompose $\boldsymbol{E}$ into components $\boldsymbol{A}$ (spanning the active space of the $\nabla\times$ operator) and $\nabla\phi$ (spanning the null space of the $\nabla\times$ operator). The resulting decomposition in Ω is

$$\boldsymbol{E} = \boldsymbol{A} + \nabla\phi, \tag{3a}$$
$$\nabla\cdot\boldsymbol{A} = 0, \tag{3b}$$

where (3b) is known as the *Coulomb gauge condition* [12]. The choice of Coulomb gauge for our work is important because it greatly simplifies the differential equations to be solved.

To get an idea of how smooth these potential fields are, consider the conditions $\boldsymbol{A}$ and ϕ must satisfy at the interface between distinct conducting media. We find these conditions by integrating over infinitesimal Gaussian pill-boxes or rectangular loops at the interface (see, e.g., [30]). With ($\boldsymbol{A}_1, \phi_1$, $\widehat{\sigma}_1$, ϵ_1) and ($\boldsymbol{A}_2, \phi_2$, $\widehat{\sigma}_2$, ϵ_2) denoting values of the corresponding quantities on opposing sides of the interface, we have

$$\boldsymbol{n}\times(\boldsymbol{A}_1 - \boldsymbol{A}_2) = 0, \tag{4a}$$
$$\boldsymbol{n}\cdot(\boldsymbol{A}_1 - \boldsymbol{A}_2) = 0, \tag{4b}$$
$$\boldsymbol{n}\cdot(\epsilon_1\nabla\phi_1 - \epsilon_2\nabla\phi_2) = \rho_s, \tag{4c}$$
$$\boldsymbol{n}\cdot(\widehat{\sigma}_1(\boldsymbol{A}_1 + \nabla\phi_1) - \widehat{\sigma}_2(\boldsymbol{A}_2 + \nabla\phi_2)) = 0, \tag{4d}$$

where $\boldsymbol{n}$ is a unit vector normal to the interface and ρ_s in (4c) is a surface charge density. We define the *generalized current density* $\widehat{\boldsymbol{J}}$ to be

$$\widehat{\boldsymbol{J}} = \widehat{\sigma}\boldsymbol{E} = (\sigma - \imath\omega\epsilon)\boldsymbol{E}. \tag{5}$$

The conditions (4) and the differential equations (1) imply that $\widehat{\boldsymbol{J}}\cdot\boldsymbol{n}$ is continuous, but $\boldsymbol{E}\cdot\boldsymbol{n}$ is not. Moreover, $\frac{\partial\phi}{\partial n}$ inherits the discontinuity of $\boldsymbol{E}\cdot\boldsymbol{n}$, while $\boldsymbol{A}$ is continuous, and both $\nabla\cdot\boldsymbol{A}$ and $\nabla\times\boldsymbol{A}$ are bounded (cf. [14]).

We can substitute (3a) into (2), and for constant μ we obtain

$$\nabla\times\nabla\times\boldsymbol{A} - \imath\omega\mu\widehat{\sigma}(\boldsymbol{A} + \nabla\phi) = \imath\omega\mu\boldsymbol{J^s}.$$

Since $\boldsymbol{A}$ is divergence-free,

$$\nabla\times\nabla\times\boldsymbol{A} \equiv -\nabla^2\boldsymbol{A} \qquad \text{in } H^{-1}(\Omega)^3 \tag{6}$$

(see Remark 3.8 and Theorem 3.5 in [14]). Using this identity and substituting (3b), we obtain

$$\nabla^2\boldsymbol{A} + \imath\omega\mu\widehat{\sigma}(\boldsymbol{A} + \nabla\phi) = -\imath\omega\mu\boldsymbol{J^s}. \tag{7}$$

Notice we cannot substitute $\nabla \times \nabla \times \boldsymbol{E} = -\nabla^2 \boldsymbol{E} + \nabla(\nabla \cdot \boldsymbol{E})$ directly because the field $\boldsymbol{E}$ is discontinuous in its normal component across interfaces between media with different conductivities. Also, if μ varies, then (6) cannot be applied and (7) does not hold. A generalization can be found [16]; however, the method proposed here is particularly fast, taking advantage of the sparsity afforded by the discretization of (7), which is not obtained unless μ is constant.

To get a diagonally dominant system, we can apply the operator $\nabla\cdot$ to (7), thereby obtaining a diffusion equation for ϕ (as in [21, 12, 4, 1]). However, $\widehat{\sigma}\boldsymbol{A} \cdot \boldsymbol{n}$ and $\widehat{\sigma}\nabla\phi \cdot \boldsymbol{n}$ can be discontinuous even though $\widehat{\boldsymbol{J}} \cdot \boldsymbol{n}$ is continuous at an interface. Therefore, differentiating the components $\widehat{\sigma}\boldsymbol{A}$ and $\widehat{\sigma}\nabla\phi$ of $\widehat{\boldsymbol{J}}$ *individually* should be avoided. We can, however, take the divergence of $\widehat{\boldsymbol{J}}$ at an interface without fear. This yields the (inhomogeneous) system of equations

$$\nabla^2 \boldsymbol{A} + \imath\omega\mu\widehat{\boldsymbol{J}} = -\imath\omega\mu\boldsymbol{J^s}, \tag{8a}$$

$$\widehat{\sigma}(\boldsymbol{A} + \nabla\phi) - \widehat{\boldsymbol{J}} = \boldsymbol{0}, \tag{8b}$$

$$\nabla \cdot \widehat{\boldsymbol{J}} = -\nabla \cdot \boldsymbol{J^s}. \tag{8c}$$

The introduction of $\widehat{\boldsymbol{J}}$ into (8) is akin to mixed finite element methods [8] which are commonly used for highly discontinuous problems.

Notice, although (3b) is left out of (8), this gauge condition is satisfied by the exact solution of (8) provided it holds at the boundaries. We avoid discretizing (3b) directly.

A simple set of BCs for the system of PDEs (8) is given by

$$-(\nabla \times \boldsymbol{A}) \times \boldsymbol{n}\Big|_{\partial\Omega} = \boldsymbol{0}, \tag{9a}$$

$$\boldsymbol{A} \cdot \boldsymbol{n}\Big|_{\partial\Omega} = 0, \tag{9b}$$

$$\frac{\partial\phi}{\partial n}\Big|_{\partial\Omega} = 0, \tag{9c}$$

$$\int_\Omega \phi \, dV = 0. \tag{9d}$$

These conditions yield a unique solution $(\boldsymbol{A}, \phi, \widehat{\boldsymbol{J}})$ for the system (8), (9). In particular, the Coulomb gauge condition (3b) is satisfied in Ω, see [16].

We use (9) for problems with sources that have compact support in Ω (bearing in mind that Ω approximates an infinite domain) [2]. But problems with sources which do not have compact support (such as in the magnetotelluric case [34]) require other choices of BCs – see Section 5.

3 Deriving a discretization

Solving the forward problem is a major bottleneck for electromagnetic inverse problems in geophysical prospecting [32]. This is the application that motivates us here. For the ensuing data inversion, one envisions a 3D tensor-product grid with the conductivity constant (or slowly varying) in each cell, but potentially varying widely between cells. Thus, we consider here a discretization on such a rectangular grid. For extensions to more complex geometries, see [18, 19], or consider mixed finite elements [8, 5, 17].

To derive a discretization for the system of PDEs (8), consider first the grid in the x-direction. There are N_x cells and hence N_x+1 vertices. These are denoted as

$$\overline{\Omega}^x := \{x_{i+1/2} : x_{1/2} < x_{3/2} < \cdots < x_{N_x+1/2},\ i = 0, \ldots, N_x\}, \tag{10a}$$

with the corresponding dual grid defined as

$$\begin{aligned} \overline{\Omega}^{x'} &:= \{x_i : i = 0, \ldots, N_x+1\}, \text{ where} \\ x_i &:= \begin{cases} x_{1/2}, & i = 0; \\ \frac{1}{2}(x_{i-1/2} + x_{i+1/2}), & i = 1, \ldots, N_x; \\ x_{N_x+1/2}, & i = N_x+1 \end{cases} . \end{aligned} \tag{10b}$$

The dual grid $\overline{\Omega}^{x'}$ gives the x-coordinates of the centers of the cells of the grid. The primary and dual grid spacings are given by

$$h^x_a := x_{a+\frac{1}{2}} - x_{a-\frac{1}{2}} \quad (a = 1/2, 1, 3/2, \ldots, N_x, N_x+1/2). \tag{10c}$$

One-dimensional grids are similarly defined in the y- and z-directions, respectively yielding $\overline{\Omega}^y$ (with N_y+1 points), $\overline{\Omega}^z$ (with N_z+1 points) and the

[2]This idea is similar to the implementation of open BCs in the context of computational fluid dynamic, see [15, 31].

corresponding dual grids $\overline{\Omega}^{y'}$ and $\overline{\Omega}^{z'}$ as in (10b). The grid spacings h_b^y and h_c^z are as in (10c). We also define the boxes

$$\begin{aligned} V_{a,b,c} &:= \left[x_{a-\frac{1}{2}}, x_{a+\frac{1}{2}}\right] \times \left[y_{b-\frac{1}{2}}, y_{b+\frac{1}{2}}\right] \times \left[z_{c-\frac{1}{2}}, z_{c+\frac{1}{2}}\right], \\ |V_{a,b,c}| &:= h_a^x h_b^y h_c^z, \ (a = 1/2, 1, \ldots, N_x + 1/2; \\ &\qquad b = 1/2, 1, \ldots, N_y + 1/2; \quad c = 1/2, 1, \ldots, N_z + 1/2) \end{aligned}$$

which are the finite-volumes over which the individual equations of (8) are integrated.

Thus, the domain for the discretization is essentially the grid

$$\overline{\Omega}^h := \overline{\Omega}^x \times \overline{\Omega}^y \times \overline{\Omega}^z.$$

The vertices of $\overline{\Omega}^h$ are the corners of $N_x N_y N_z$ boxes that constitute the cells of the grid (as seen in Figure 1). That is, the cell $V_{i,j,k}$ is the box with eight corners $(x_{i\pm\frac{1}{2}}, y_{j\pm\frac{1}{2}}, z_{k\pm\frac{1}{2}})$ and center (x_i, y_j, z_k) ($i = 1, \ldots, N_x$, $j = 1, \ldots, N_y$, $k = 1, \ldots, N_z$). The centers of the six faces of the cell $V_{i,j,k}$ are the six points $(x_{i\pm\frac{1}{2}}, y_j, z_k)$, $(x_i, y_{j\pm\frac{1}{2}}, z_k)$, and $(x_i, y_j, z_{k\pm\frac{1}{2}})$. Furthermore, within each cell $V_{i,j,k}$, the conductivity σ varies smoothly or is constant with $\sigma \equiv \sigma_{i,j,k}$ throughout the cell. However, σ may be discontinuous between adjacent cells. The permittivity ϵ is represented in the same way as σ (ie. with $\epsilon \equiv \epsilon_{i,j,k}$ throughout $V_{i,j,k}$), although the variations in ϵ are much less than those in σ. Thus, the domain is composed of blocks of distinct conducting materials.

Having defined the grid, we now identify where the grid functions approximating $\boldsymbol{A}$, $\widehat{\boldsymbol{J}}$ and ϕ are defined. Basically, both vector fields $\boldsymbol{A}$ and $\widehat{\boldsymbol{J}}$ are approximated in each cell using the approximate values of the normal components of the fields at the center of each face. The scalar field ϕ is approximated in each cell using the approximate value of ϕ at the center of the cell. Denoting $\boldsymbol{A} \equiv (A^x, A^y, A^z)^T$ and $\widehat{\boldsymbol{J}} \equiv (\widehat{J^x}, \widehat{J^y}, \widehat{J^z})^T$, the locations of the grid functions are shown in Table 1 and Figure 1.

To approximate (8c), we integrate at first over the box $V_{i,j,k}$ using Gauss' divergence theorem

$$\frac{1}{|V_{i,j,k}|} \int_{V_{i,j,k}} \nabla \cdot \widehat{\boldsymbol{J}} \, dV = \frac{1}{|V_{i,j,k}|} \int_{\partial V_{i,j,k}} \widehat{\boldsymbol{J}} \cdot \boldsymbol{n} \, dS.$$

Using midpoint quadrature on each face to evaluate each of the surface integrals on the right-hand side above, we find the discrete equation correspond-

$$\boxed{\begin{array}{ll} {A^x}_{i+\frac{1}{2},j,k} \approx A^x(x_{i+\frac{1}{2}}, y_j, z_k) & {\widehat{J^x}}_{i+\frac{1}{2},j,k} \approx \widehat{J^x}(x_{i+\frac{1}{2}}, y_j, z_k) \\ {A^y}_{i,j+\frac{1}{2},k} \approx A^y(x_i, y_{j+\frac{1}{2}}, z_k) & {\widehat{J^y}}_{i,j+\frac{1}{2},k} \approx \widehat{J^y}(x_i, y_{j+\frac{1}{2}}, z_k) \\ {A^z}_{i,j,k+\frac{1}{2}} \approx A^z(x_i, y_j, z_{k+\frac{1}{2}}) & {\widehat{J^z}}_{i,j,k+\frac{1}{2}} \approx \widehat{J^z}(x_i, y_j, z_{k+\frac{1}{2}}) \\ \multicolumn{2}{c}{\phi_{i,j,k} \approx \phi(x_i, y_j, z_k)} \end{array}}$$

Table 1: The discrete grid functions: each scalar field is approximated by the grid functions at points slightly staggered in each cell of the grid.

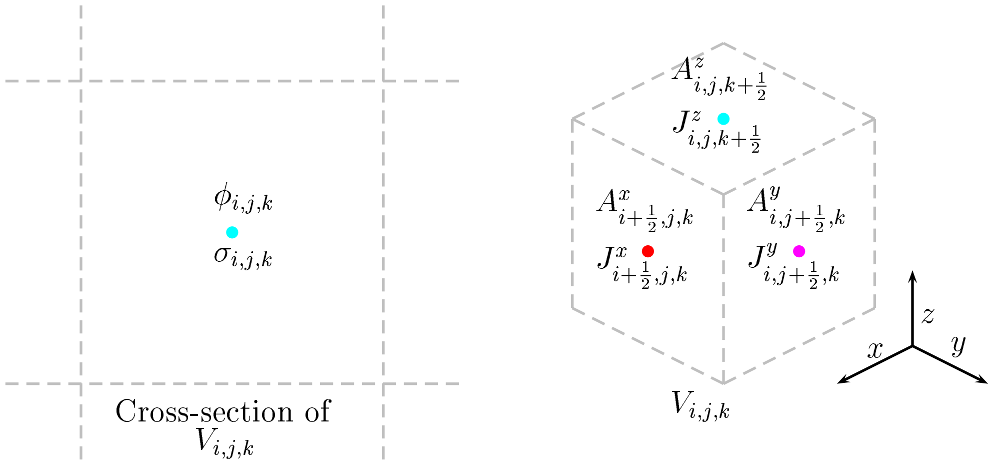

Figure 1: The cell $V_{i,j,k}$ along with a cross-section. The cell $V_{i,j,k}$ corresponds to a block of conductive material within which $\sigma \approx \sigma_{i,j,k}$.

ing to (8c),

$$\frac{{\widehat{J^x}}_{i+\frac{1}{2},j,k} - {\widehat{J^x}}_{i-\frac{1}{2},j,k}}{h^x_i} + \frac{{\widehat{J^y}}_{i,j+\frac{1}{2},k} - {\widehat{J^y}}_{i,j-\frac{1}{2},k}}{h^y_j} + \frac{{\widehat{J^z}}_{i,j,k+\frac{1}{2}} - {\widehat{J^z}}_{i,j,k-\frac{1}{2}}}{h^z_k} + \\ \frac{s^x_{i+\frac{1}{2},j,k} - s^x_{i-\frac{1}{2},j,k}}{h^x_i} + \frac{s^y_{i,j+\frac{1}{2},k} - s^y_{i,j-\frac{1}{2},k}}{h^y_j} + \frac{s^z_{i,j,k+\frac{1}{2}} - s^z_{i,j,k-\frac{1}{2}}}{h^z_k} = 0, \tag{11}$$

where we denote $\boldsymbol{J^s} = (s^x, s^y, s^z)^T$.

Next, consider, say, the x-component of (8b), written as

$$\frac{\partial \phi}{\partial x} = -A^x + \widehat{\sigma}^{-1}\widehat{J^x},$$

i.e. as an equality of possibly discontinuous quantities. Integrating this equation on the line segment from (x_i, y_j, z_k) to (x_{i+1}, y_j, z_k), we cross a boundary between cells and hence encounter possible discontinuities in $\widehat{\sigma}$ and $\frac{\partial \phi}{\partial x}$. However, integration is a smoothing operation, so the result of this integration is well-defined. We define the *harmonic average* of the conductivity between the neighboring cells by

$$\widehat{\sigma}_{i+\frac{1}{2},j,k} = h^x_{i+\frac{1}{2}} \left(\int_{x_i}^{x_{i+1}} \widehat{\sigma}^{-1}(x, y, z) dx \right)^{-1}. \tag{12a}$$

If $\widehat{\sigma}$ is assumed to be constant over each cell, this integral evaluates to

$$\widehat{\sigma}_{i+\frac{1}{2},j,k} = h^x_{i+\frac{1}{2}} \left(\frac{h^x_i}{2\widehat{\sigma}_{i,j,k}} + \frac{h^x_{i+1}}{2\widehat{\sigma}_{i+1,j,k}} \right)^{-1}. \tag{12b}$$

Then, the resulting approximation for the x-component of (8b) is

$$\widehat{J^x}_{i+\frac{1}{2},j,k} = \widehat{\sigma}_{i+\frac{1}{2},j,k} \left({A^x}_{i+\frac{1}{2},j,k} + \frac{\phi_{i+1,j,k} - \phi_{i,j,k}}{h^x_{i+\frac{1}{2}}} \right). \tag{12c}$$

The above derivation using harmonic – rather than arithmetic – averages is natural in our approach upon applying numerical considerations alone (viz. integrating rough quantities). Using harmonic averages as indicated becomes important in practice when jumps by a few orders of magnitude in conductivity are present. Harmonic averaging is also natural on physical grounds, as it corresponds to serial, rather than parallel, current flow (see, e.g., [28]).

Using (12c) and similar expressions derived in the y- and z-directions, we eliminate $\widehat{\boldsymbol{J}}$ from (11) and obtain a discrete equation in which the dominant terms all involve ϕ. The resulting stencil for ϕ has 7 points.

There are two ways to view the procedure of eliminating $\widehat{\boldsymbol{J}}$. Firstly, it is an algebraic manipulation (a Schur decomposition) which reduces the number of unknowns. Secondly, the result of the elimination corresponds to a compact discretization of

$$\nabla \cdot (\widehat{\sigma} \nabla \phi) + \nabla \cdot (\widehat{\sigma} \boldsymbol{A}) = -\nabla \cdot \boldsymbol{J^s}. \tag{13}$$

However, this correspondence holds only if the terms on the left-hand side of (13) exist (i.e., if $\widehat{\sigma}$ is smooth; for a similar idea in a different context, see [15]). Our discretization yields a valid approximation for the solution of (8b)-(8c) even if the individual terms in (13) are unbounded!

It is natural (although not necessary) to define $\boldsymbol{A}$ at the same spatial locations where $\widehat{\boldsymbol{J}}$ is defined, as depicted in Figure 1. The discretization of the components of (8a) is obtained using a standard 7-point stencil to approximate the Laplacian operator or through a finite volume discretization of

$$-\nabla \times \nabla \times \boldsymbol{A} + \nabla(\nabla \cdot \boldsymbol{A}) + \imath\omega\mu\widehat{\boldsymbol{J}} = -\imath\omega\mu\boldsymbol{J}^{\boldsymbol{s}}$$

(see [16]) which yields the same discrete equations. This completes the derivation of the discretization for a general, tensor-product non-uniform grid. The same finite-volume arguments are used to determine how Dirichlet or Neumann BCs fit into the stencils near the boundaries. Our treatment of the BCs follows the one described by Fletcher [13].

In summary, the discretization of (8) on a uniform grid with spacing $h_i^x = h_j^y = h_k^z \equiv h$ is

$$\begin{aligned} h^{-2}(&{A^x}_{i+\frac{3}{2},j,k} + {A^x}_{i+\frac{1}{2},j+1,k} + {A^x}_{i+\frac{1}{2},j,k+1} + \\ &{A^x}_{i-\frac{1}{2},j,k} + {A^x}_{i+\frac{1}{2},j-1,k} + {A^x}_{i+\frac{1}{2},j,k-1} - \\ &6{A^x}_{i+\frac{1}{2},j,k}) + \imath\omega\mu\widehat{J^x}_{i+\frac{1}{2},j,k} = -\imath\omega\mu\, s^x_{i+\frac{1}{2},j,k}, \end{aligned} \tag{14a}$$

$$\begin{aligned} h^{-2}(&{A^y}_{i+1,j+\frac{1}{2},k} + {A^y}_{i,j+\frac{3}{2},k} + {A^y}_{i,j+\frac{1}{2},k+1} + \\ &{A^y}_{i-1,j+\frac{1}{2},k} + {A^y}_{i,j-\frac{1}{2},k} + {A^y}_{i,j+\frac{1}{2},k-1} - \\ &6{A^y}_{i,j+\frac{1}{2},k}) + \imath\omega\mu\widehat{J^y}_{i,j+\frac{1}{2},k} = -\imath\omega\mu\, s^y_{i,j+\frac{1}{2},k}, \end{aligned} \tag{14b}$$

$$\begin{aligned} h^{-2}(&{A^z}_{i+1,j,k+\frac{1}{2}} + {A^z}_{i,j+1,k+\frac{1}{2}} + {A^z}_{i,j,k+\frac{3}{2}} + \\ &{A^z}_{i-1,j,k+\frac{1}{2}} + {A^z}_{i,j-1,k+\frac{1}{2}} + {A^z}_{i,j,k-\frac{1}{2}} - \\ &6{A^z}_{i,j,k+\frac{1}{2}}) + \imath\omega\mu\widehat{J^z}_{i,j,k+\frac{1}{2}} = -\imath\omega\mu\, s^z_{i,j,k+\frac{1}{2}}, \end{aligned} \tag{14c}$$

$$
\begin{aligned}
h^{-2}&(\widehat{\sigma}_{i+\frac{1}{2},j,k}(\phi_{i+1,j,k}-\phi_{i,j,k})-\widehat{\sigma}_{i-\frac{1}{2},j,k}(\phi_{i,j,k}-\phi_{i-1,j,k})+\\
&\widehat{\sigma}_{i,j+\frac{1}{2},k}(\phi_{i,j+1,k}-\phi_{i,j,k})-\widehat{\sigma}_{i,j-\frac{1}{2},k}(\phi_{i,j,k}-\phi_{i,j-1,k})+\\
&\widehat{\sigma}_{i,j,k+\frac{1}{2}}(\phi_{i,j,k+1}-\phi_{i,j,k})-\widehat{\sigma}_{i,j,k-\frac{1}{2}}(\phi_{i,j,k}-\phi_{i,j,k-1}))+\\
h^{-1}&(\widehat{\sigma}_{i+\frac{1}{2},j,k}{A^x}_{i+\frac{1}{2},j,k}+\widehat{\sigma}_{i,j+\frac{1}{2},k}{A^y}_{i,j+\frac{1}{2},k}+\widehat{\sigma}_{i,j,k+\frac{1}{2}}{A^z}_{i,j,k+\frac{1}{2}}-\\
&\widehat{\sigma}_{i-\frac{1}{2},j,k}{A^x}_{i-\frac{1}{2},j,k}-\widehat{\sigma}_{i,j-\frac{1}{2},k}{A^y}_{i,j-\frac{1}{2},k}-\widehat{\sigma}_{i,j,k-\frac{1}{2}}{A^z}_{i,j,k-\frac{1}{2}})\\
&= \quad h^{-1}(s^x_{i+\frac{1}{2},j,k}+s^y_{i,j+\frac{1}{2},k}+s^z_{i,j,k+\frac{1}{2}}-\\
&\qquad\qquad s^x_{i-\frac{1}{2},j,k}-s^y_{i,j-\frac{1}{2},k}-s^z_{i,j,k-\frac{1}{2}}),
\end{aligned}
\tag{14d}
$$

where the components of $\widehat{\boldsymbol{J}}$ can be eliminated by

$$
\begin{aligned}
\widehat{J^x}_{i+\frac{1}{2},j,k} &= h^{-1}\widehat{\sigma}_{i+\frac{1}{2},j,k}(\phi_{i+1,j,k}-\phi_{i,j,k})\\
&\quad+\widehat{\sigma}_{i+\frac{1}{2},j,k}{A^x}_{i+\frac{1}{2},j,k}, && \text{(14e)}\\
\widehat{J^y}_{i,j+\frac{1}{2},k} &= h^{-1}\widehat{\sigma}_{i,j+\frac{1}{2},k}(\phi_{i,j+1,k}-\phi_{i,j,k})\\
&\quad+\widehat{\sigma}_{i,j+\frac{1}{2},k}{A^y}_{i,j+\frac{1}{2},k}, && \text{(14f)}\\
\widehat{J^z}_{i,j,k+\frac{1}{2}} &= h^{-1}\widehat{\sigma}_{i,j,k+\frac{1}{2}}(\phi_{i,j,k+1}-\phi_{i,j,k})\\
&\quad+\widehat{\sigma}_{i,j,k+\frac{1}{2}}{A^z}_{i,j,k+\frac{1}{2}}. && \text{(14g)}
\end{aligned}
$$

The introduction of $\widehat{\boldsymbol{J}}$ into the formulation (8) makes it easy to generate a point-wise accurate approximation to the (possibly discontinuous) electric field $\boldsymbol{E}$ with our discretization (14). Usually, the fields $\boldsymbol{A}$ and ϕ are computed solely for the purpose of calculating $\boldsymbol{E}$ and $\boldsymbol{H}$ in post-processing; thus, computing $\boldsymbol{E}$ directly from (3a) (as suggested in [1, 20, 24, 12, 21]) involves a loss of accuracy due to numerical differentiation to obtain a possibly discontinuous $\nabla\phi$. We avoid this loss of accuracy by calculating $\widehat{\boldsymbol{J}}$ (which is continuous) at the grid points where $\boldsymbol{A}$ is defined using (14e)–(14g), and then determining $\boldsymbol{E}$ using (5). Thus, the electric field can be accurately determined at either side of the boundary which separates media having different conductivities.

3.1 Conservation of vector identities and relationship with Yee's method

On the (non-uniform) staggered grid, we can define natural discrete difference operators that involve only "short" difference quotients: $\nabla\cdot_h$ as used in (11) for $\nabla \cdot \widehat{\boldsymbol{J}}$; ∇_h as used in (12c) for $\nabla\phi$, ∇_h^2 as used in (14) for $\nabla^2 \boldsymbol{A}$; and $\nabla \times_h$ as used in (16) below. It is then easy to verify that the following discrete vector identities hold in the grid's interior, reproducing the continuous vector identities (cf. [18, 9]):

$$(\nabla \times_h)\nabla_h = \mathbf{0}, \tag{15a}$$

$$(\nabla \cdot_h)(\nabla \times_h) = 0, \tag{15b}$$

$$\nabla_h(\nabla \cdot_h) - (\nabla \times_h)(\nabla \times_h) = \nabla_h^2, \tag{15c}$$

$$\nabla \cdot_h \Phi = 0 \Rightarrow \nabla \cdot_h \nabla_h^2 \Phi = 0. \tag{15d}$$

In electromagnetic modeling, it is common to use Yee's method [35]. As mentioned in the introduction, most implementations of this method define the tangential component of $\boldsymbol{E}$ along the edges of a grid cell (or a finite volume) and the normal components of $\boldsymbol{H}$ at the facial interfaces; see, e.g., [25]. However, this is not a fundamental requirement. In fact, our method is more closely associated with a modification of Yee's discretization with normal components of $\boldsymbol{E}$ defined on the cell faces and tangential components of $\boldsymbol{H}$ defined on the edges. This requires appropriate field substitutions and definitions of conductivity. We do so below and relate the resulting equations to those from our derivation.

Consider Yee's discretization, applied to (1a,b) for a uniform grid as in (14). The placement of the various discrete solution components on the cell is depicted in Figure 2.

The centered discretization is

$$\begin{aligned} h^{-1}\left({E^z}_{i,j+1,k+\frac{1}{2}} - {E^z}_{i,j,k+\frac{1}{2}} - {E^y}_{i,j+\frac{1}{2},k+1} + {E^y}_{i,j+\frac{1}{2},k}\right) \\ - \imath\omega\mu {H^x}_{i,j+\frac{1}{2},k+\frac{1}{2}} = 0, \end{aligned} \tag{16a}$$

$$\begin{aligned} h^{-1}\left({E^x}_{i+\frac{1}{2},j,k+1} - {E^x}_{i+\frac{1}{2},j,k} - {E^z}_{i+1,j,k+\frac{1}{2}} + {E^z}_{i,j,k+\frac{1}{2}}\right) \\ - \imath\omega\mu {H^y}_{i+\frac{1}{2},j,k+\frac{1}{2}} = 0, \end{aligned} \tag{16b}$$

$$\begin{aligned} h^{-1}\left({E^y}_{i+1,j+\frac{1}{2},k} - {E^y}_{i,j+\frac{1}{2},k} - {E^x}_{i+\frac{1}{2},j+1,k} + {E^x}_{i+\frac{1}{2},j,k}\right) \\ - \imath\omega\mu {H^z}_{i+\frac{1}{2},j+\frac{1}{2},k} = 0, \end{aligned} \tag{16c}$$

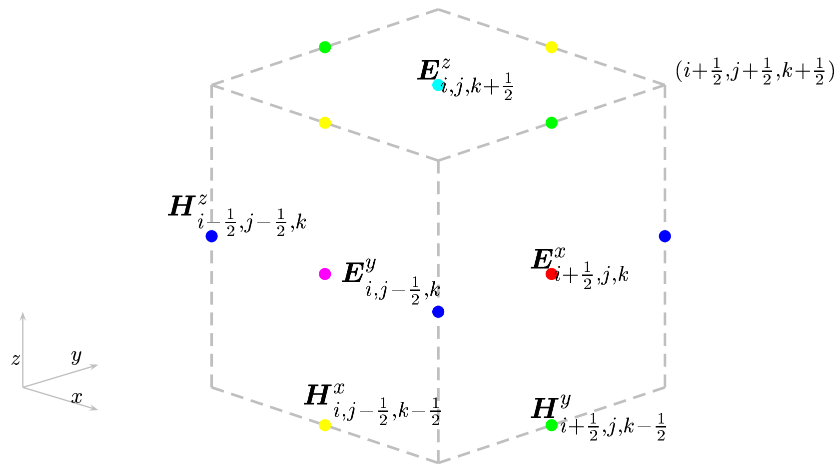

Figure 2: Staggered discretization of $\boldsymbol{E}$ and $\boldsymbol{H}$ in three dimensions.

$$h^{-1}\left({H^z}_{i+\frac12,j+\frac12,k} - {H^z}_{i+\frac12,j-\frac12,k} - {H^y}_{i+\frac12,j,k+\frac12} + {H^y}_{i+\frac12,j,k-\frac12}\right)$$
$$- \widehat{\sigma}_{i+\frac12,j,k}{E^x}_{i+\frac12,j,k} = s^x_{i+\frac12,j,k}, \tag{16d}$$

$$h^{-1}\left({H^x}_{i,j+\frac12,k+\frac12} - {H^x}_{i,j+\frac12,k-\frac12} - {H^z}_{i+\frac12,j+\frac12,k} + {H^z}_{i-\frac12,j+\frac12,k}\right)$$
$$- \widehat{\sigma}_{i,j+\frac12,k}{E^y}_{i,j+\frac12,k} = s^y_{i,j+\frac12,k}, \tag{16e}$$

$$h^{-1}\left({H^y}_{i+\frac12,j,k+\frac12} - {H^y}_{i-\frac12,j,k+\frac12} - {H^x}_{i,j+\frac12,k+\frac12} + {H^x}_{i,j-\frac12,k+\frac12}\right)$$
$$- \widehat{\sigma}_{i,j,k+\frac12}{E^z}_{i,j,k+\frac12} = s^z_{i,j,k+\frac12}. \tag{16f}$$

In (16), we have not defined the quantities $\widehat{\sigma}_{i+\frac12,j,k}$, $\widehat{\sigma}_{i,j+\frac12,k}$, and $\widehat{\sigma}_{i,j,k+\frac12}$, nor have we resolved the possible discontinuities in $\boldsymbol{E}\cdot\boldsymbol{n}$ across cells (for example, ${E^x}_{i+\frac12,j,k}$ may have different limiting values in the cell $V_{i,j,k}$ and the cell $V_{i+1,j,k}$). We now address both these points using our previously introduced approach.

1. We can eliminate the components of $\boldsymbol{H}$ unambiguously by substituting (16a–c) into (16d–f). This algebraic elimination corresponds exactly to discretizing the second-order system (2) in $\boldsymbol{E}$. In particular, it is a compact discretization for each of the components of $\boldsymbol{E}$ on the staggered grid.

2. Next, we introduce the decomposition (3). This resolves the ambiguity in $\boldsymbol{E}$ on the cell faces in case of discontinuities and handles the null space of the $\nabla\times$ operator. The natural discretization is

$$\begin{aligned} {E^x}_{i+\frac{1}{2},j,k} &= {A^x}_{i+\frac{1}{2},j,k} + h^{-1}(\phi_{i+1,j,k} - \phi_{i,j,k}), \\ {E^y}_{i,j+\frac{1}{2},k} &= {A^y}_{i,j+\frac{1}{2},k} + h^{-1}(\phi_{i,j+1,k} - \phi_{i,j,k}), \\ {E^z}_{i,j,k+\frac{1}{2}} &= {A^z}_{i,j,k+\frac{1}{2}} + h^{-1}(\phi_{i,j,k+1} - \phi_{i,j,k}). \end{aligned}$$

This leads to the staggered grid definition as in Figure 1.

Substituting into (16), note that according to (15a), the contributions corresponding to $\nabla \times \nabla\phi$ vanish. Further, we *require*

$$\begin{aligned} \nabla \cdot {}_h\boldsymbol{A}_{i,j,k} &= h^{-1}\Big({A^x}_{i+\frac{1}{2},j,k} - {A^x}_{i-\frac{1}{2},j,k} + {A^y}_{i,j+\frac{1}{2},k} - {A^y}_{i,j-\frac{1}{2},k} \\ &\qquad + {A^z}_{i,j,k+\frac{1}{2}} - {A^z}_{i,j,k-\frac{1}{2}}\Big) = 0. \end{aligned} \tag{17}$$

Then, using (15d), we obtain our equations (14) from Yee's method.

3. Finally, we are able to naturally and carefully derive an expression for σ on cell faces using harmonic averages, as in (12).

Remember in our method, we do not explicitly impose (17). However, these equations are consistent with our discretization if the BCs with which the PDE system (8) is equipped are such that (3b) is satisfied everywhere (as is the case with (9)). In such a case our discretization yields the same solution as Yee's method with the definition (12) (which holds even when $\nabla\phi$ is discontinuous). We have arrived at a correct way of extending Yee's method (16) in order to overcome both the presence of discontinuities in σ and the slow convergence of iterative methods for the algebraic equations! If the BCs for (8) reproduce (3b) only approximately, then the methods yield different solutions; see Section 5.

4 Numerical solution of the discrete system

Even after eliminating $\widehat{\boldsymbol{J}}$, the system (8) has four unknown scalar fields defined over a three-dimensional domain. The resulting discrete system derived in Section 3 is typically very large and sparse, so we use preconditioned

Krylov space methods for its solution [27, 2]. As in [1], the discretized equations can be written as

$$\begin{pmatrix} \frac{1}{\omega\mu}H_1 & & & \imath S_1 G_1 \\ & \frac{1}{\omega\mu}H_2 & & \imath S_2 G_2 \\ & & \frac{1}{\omega\mu}H_3 & \imath S_3 G_3 \\ D_1 S_1 & D_2 S_2 & D_3 S_3 & L \end{pmatrix} \begin{pmatrix} A_1 \\ A_2 \\ A_3 \\ \phi \end{pmatrix} = \begin{pmatrix} b_1 \\ b_2 \\ b_3 \\ b_\phi \end{pmatrix}. \tag{18}$$

Here, H_1, H_2 and H_3 are discretizations of the (complex) Helmholtz operators; $(G_1, G_2, G_3)^T$ is a discretization of the operator ∇; (D_1, D_2, D_3) is a discretization of the operator $\nabla\cdot$; (S_1, S_2, S_3) is a discretization of the operator $\widehat{\sigma}(\cdot)$; and L is a discretization of the operator $\nabla\cdot(\widehat{\sigma}\nabla(\cdot))$. In this case, H_1, H_2 and H_3 are distinct matrices due to the staggered grid; this is a drawback compared to [1].

The block structure of the matrix in (18) holds for our staggered discretization (14), but not for (16) nor for discretizations that directly involve (3b). The diagonal blocks H_1, H_2, H_3 and L are discretizations of second-order differential operators and are therefore the dominant blocks of the system. Furthermore, although the system (18) is larger than the system arising from the direct discretization of (2), it has roughly the same number of nonzero entries because the discretization of the operator $\nabla\times\nabla\times$ involves 13 points, whereas that for ∇^2 involves only 7 points.

As in [1], we solve (18) using BICGSTAB with a block incomplete-LU (ILU) preconditioner [2]. A modest improvement can be made by separating the system (18) into its real and imaginary parts, since the imaginary part appears only in the low-order terms of (1). Furthermore, the real part of the Helmholtz operator corresponds to the dielectric permittivity and the imaginary part corresponds to the conductivity. The result is the real system

$$\begin{pmatrix} H_\epsilon & S_\epsilon G & -S_\sigma & -S_\sigma G \\ DS_\sigma & DS_\sigma G & DS_\epsilon & DS_\epsilon G \\ S_\sigma & S_\sigma G & H_\epsilon & S_\epsilon G \\ -DS_\epsilon & -DS_\epsilon G & DS_\sigma & DS_\sigma G \end{pmatrix} \begin{pmatrix} \boldsymbol{A}_{re} \\ \phi_{re} \\ \boldsymbol{A}_{im} \\ \phi_{im} \end{pmatrix} = \begin{pmatrix} \boldsymbol{b}_{re} \\ b_{\phi_{re}} \\ \boldsymbol{b}_{im} \\ b_{\phi_{im}} \end{pmatrix}, \tag{19}$$

where the matrix H_ϵ is the discretization of the 3D Helmholtz operator (which depends on the permeability, ϵ, and the frequency, ω), S_σ and S_ϵ are diagonal matrices that discretize the three components of the operators $\sigma(\cdot)$ and $\omega\epsilon(\cdot)$ and G and D are the discrete representations of ∇ and $\nabla\cdot$. In (19), the matrix blocks have the form

$$
\begin{aligned}
&H_\epsilon = (\omega\mu)^{-1}\nabla_h^2 + S_\epsilon, && \nabla_h^2 = \mathrm{diag}(\nabla_x^2, \nabla_y^2, \nabla_z^2), \\
&S_\sigma = \mathrm{diag}(S_{\sigma x}, S_{\sigma y}, S_{\sigma z}), && S_\epsilon = \mathrm{diag}(S_{\epsilon x}, S_{\epsilon y}, S_{\epsilon z}), \\
&G = (G_1, G_2, G_3)^T, && D = (D_1, D_2, D_3).
\end{aligned} \tag{20}
$$

In (20), ∇_p^2 is the (discrete) Laplacian operator for the pth component of a vector field, and $S_{\epsilon p}$ and $S_{\sigma p}$ are likewise discrete approximations of ϵI and σI, respectively, on the appropriate faces of the staggered grid ($p = x, y, z$).

For sufficiently fine grids, the Laplacian blocks are dominant in their respective rows and columns, whence the system is diagonally dominant. The convergence of Krylov space solvers relates directly to the diagonal dominance of the system (19). For the preconditioning of the blocks H_1, H_2 and H_3 of (18) or (19), we can use ILU(0), i.e., no fill-in allowed. However, for the blocks $DS_\sigma G$, which are more complicated due to the discontinuities in σ, we use ILU with threshold 10^{-3}; see [27]. The ILU code we use is taken from [27] as well.

5 Numerical Experiments and Results

For the calculations reported in this section, we assume the quasi-static approximation holds, so $\widehat{\sigma} \equiv \sigma$ as in [1]. The boundary conditions (BCs) are different from (9) because we attempt to model the magnetotelluric (MT) experiment [32]. This experiment involves fields driven by a source which has no compact support in an unbounded domain. Upon considering the approximate problem on a finite domain Ω, there are different ways to impose BCs on the finite domain boundary, $\partial\Omega$, when modelling this experiment. For instance, in [22], $\boldsymbol{E}|_{\partial\Omega}$ is prescribed, while in [26], $\boldsymbol{H}$ and $\boldsymbol{E}$ are prescribed on different portions of the boundary.

In our modelling, we prescribe BCs directly on $\boldsymbol{A}$ and ϕ based on their physical interpretation[3]. We assume that there are no charge sources at infinity. Thus, for a sufficiently large rectangular domain of the form

$$\Omega := [-L_x, L_x] \times [-L_y, L_y] \times [-L_z, L_z] \tag{21}$$

[3] Recall from [1] that ϕ is generated from accumulated charges while $\boldsymbol{A}$ arises from time varying magnetic fields.

ϕ arises only from charge accumulation at conductivity discontinuities which are well inside Ω and far from its boundary. Therefore, $\nabla\phi|_{\partial\Omega} \approx \mathbf{0}$ and correspondingly $\boldsymbol{E}|_{\partial\Omega} \approx \boldsymbol{A}|_{\partial\Omega}$.

We require

$$\left.\frac{\partial \phi}{\partial n}\right|_{\partial\Omega} = 0, \tag{22a}$$

which guarantees a unique decomposition in (3) for a given electric field. In addition, set

$$\left.\frac{\partial \boldsymbol{A}}{\partial x}\right|_{x=\pm L_x} = \mathbf{0}, \ \left.\frac{\partial \boldsymbol{A}}{\partial y}\right|_{y=\pm L_y} = \mathbf{0}. \tag{22b}$$

Corresponding to a plane wave in an MT experiment (which has a source without compact support) we impose

$$\left.\boldsymbol{A}\right|_{z=\pm L_z} = \boldsymbol{g}(x, y, \pm L_z) \tag{22c}$$

where $\boldsymbol{g}$ is a known data function.

By fixing $\phi = 0$ at one point on the boundary, or alternatively imposing (9d), the PDE system (8),(22) is well posed. Note that (3b) no longer holds precisely, but $\|\nabla \cdot \boldsymbol{A}\|$ decreases rapidly as the domain Ω is increased.

5.1 A synthetic problem

For low-frequency, diffusive problems involving finite discontinuities, we are not aware of three-dimensional, closed form solutions of the system (8) reported in the literature. Therefore, we generate a synthetic example that allows us to test many features of the algorithm.

For the model domain we set $L_x = L_y = L_z = 1$ in (21). We define an analytic, quasi-static conductivity function depending on a parameter a,

$$\widehat{\sigma}(x, y, z) \equiv \sigma(x, y, z) = \psi_a(x)\, \psi_a(y)\, \psi_a(z), \tag{23a}$$

where

$$\psi_a(\xi) := \tanh\left(a\left(\xi + \frac{1}{4}\right)\right) - \tanh\left(a\left(\xi - \frac{1}{4}\right)\right) + \frac{1}{100}. \tag{23b}$$

The function ψ_a in (23b) varies slowly in $[-1, 1]$ except near $\xi = \pm 0.25$, where

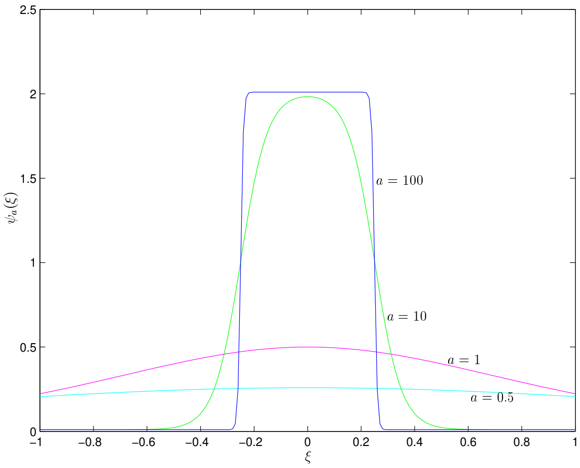

Figure 3: The function ψ_a for various values of $a > 0$: as a increases, ψ_a becomes steeper.

$|\psi_a'| \approx a$; thus, the parameter a controls the steepness of effective "jumps" in $\widehat{\sigma}$ (see Figure 3). For $0 < a \leq 1$, $\widehat{\sigma}$ is not too steep while for $a \geq 10$, $\widehat{\sigma}$ is effectively discontinuous (like a conducting block in a nonconducting material). Note that $\widehat{\sigma}$ varies over 7 orders of magnitude, roughly from 10^{-6} to 8. The directions across which $\widehat{\sigma}$ varies rapidly align with the grid.

We next choose an electric field,

$$\boldsymbol{E} = \left(\frac{-zy\ e^{-5(x^2+y^2+z^2)}}{\psi_a(x)}, \frac{-xz\ e^{-5(x^2+y^2+z^2)}}{\psi_a(y)}, \frac{-xy\ e^{-5(x^2+y^2+z^2)}}{\psi_a(z)} \right)^T . \quad (24)$$

Notice $\|\boldsymbol{E}(x,y,z)\| \to 0$ as $(x^2 + y^2 + z^2) \to \infty$. On the finite domain boundary $\|\boldsymbol{E}(x,y,z)\|$ is small: e.g. for $a = 100$, $\max_{\partial\Omega} |\boldsymbol{E}(x,y,z)| < 0.09$, which we consider an acceptable source of error. Also, for the grids used, with sufficiently large values of a (say, $a > 10$), $\boldsymbol{E}$ varies rapidly as if it has a jump discontinuity in the normal (but not tangential) directions at the "interfaces" where $\widehat{\sigma}$ changes rapidly. On the other hand, the current $\widehat{\boldsymbol{J}} = \widehat{\sigma}\boldsymbol{E}$ varies rapidly in its tangential components but not in its normal components at the same interfaces.

We set $\mu = 4\pi \cdot 10^{-7}$ H/m and $\boldsymbol{g} = \boldsymbol{0}$. The diffusion number $\omega\mu\widehat{\sigma}L^2 \approx 100$ is typical in a geophysical scenario in which the domain includes roughly seven skin depths. For the source term, we now define

$$\boldsymbol{J^s} := (\imath\omega\mu)^{-1}\nabla\times\ \nabla\times\ \boldsymbol{E} - \widehat{\sigma}\boldsymbol{E}. \tag{25}$$

The values of $\widehat{\sigma}$ on block boundaries are evaluated using harmonic averages as in Section 3. The source in (25) is not physically realistic as it lacks compact support. However, this example does provide a good test case approximating a highly discontinuous problem.

At this point we can generate the linear system (19) for a given frequency ω and find an approximate solution $(\boldsymbol{A}_h, \phi_h)^T$. Unfortunately, we do not have closed-form expressions for $(\boldsymbol{A}, \phi)$ such that (3) holds. However, we can compute a pseudo-analytical solution by solving on the same grid a similar finite volume discretization for the system

$$\begin{aligned} \boldsymbol{A} + \nabla\phi &= \boldsymbol{E}, && \text{(26a)} \\ \nabla\cdot\boldsymbol{A} &= 0, && \text{(26b)} \end{aligned}$$

together with (22a), using the analytic $\boldsymbol{E}$ from (24) on the right-hand side of (26). The differences between the numerical solutions of (19) and (26) are denoted by $\delta\boldsymbol{A}$ and $\delta\phi$.

We present a summary of results in Table 2. In addition to $\|\delta\boldsymbol{A}\|$ and $\|\delta\phi\|$, we provide $\|\delta\widehat{\boldsymbol{J}}\|$ (the difference between the analytic and computed currents) and $\|\nabla\cdot\boldsymbol{A}\|$ (the residual associated with (3b)). These differences are measured in the maximum norm and in the normalized Euclidean 2-norm.

The results in Table 2 show that the solution error generally decreases like h^2 as the grid is refined. Observe that the errors in the current (and therefore in the electric field) are $\mathcal{O}(h^2)$ because $\widehat{\boldsymbol{J}}$ is computed point-wise from the discretization of (8b) with second-order accuracy. Notice that the convergence rate does not change as the gradients in $\widehat{\sigma}$ increase in magnitude, although a finer grid is needed for comparable accuracy when the layers are sharper. This result implies that solving practical three-dimensional problems requires a sufficiently dense mesh to get meaningful results. The analytic and computed currents agree favorably as seen in Figure 4. Only the real parts are presented because, for this example, both the conductivity and the electric fields are real.

Observe that of the error indicators in Table 2, the only true solution error is $\delta\widehat{\boldsymbol{J}}$. The measured norms for $\nabla\cdot\boldsymbol{A}$, as well as the comparisons to the pseudo-analytical solution, reflect the error in using a finite domain of

# cells	h	h^2	# variables
8^3	.25	6.25e-2	4224
16^3	.125	1.56e-2	33280
32^3	.0625	3.9e-3	264192

Grid	a	M	$\|\delta \boldsymbol{A}\|$		$\|\delta\phi\|$		$\|\nabla\cdot\boldsymbol{A}\|$		$\|\delta\widehat{\boldsymbol{J}}\|$	
8^3		5	2.2	2.6e-1	2.9e-1	1.3e-1	9.2e-2	2.1e-2	7.8e-1	9.3e-2
16^3	0.5	7	3.9e-1	3.2e-2	3.8e-2	3.6e-3	6.8e-3	5.1e-4	1.8e-1	1.3e-2
32^3		12	7.8e-2	4.8e-3	9.3e-3	2.3e-3	2.4e-3	1.0e-4	1.0e-4	2.3e-3
8^3		5	2.2	2.7e-1	3.3e-1	1.6e-1	4.8e-2	4.6e-3	7.5e-1	8.8e-2
16^3	1	7	3.8e-1	3.2e-2	4.0e-2	4.1e-3	3.6e-3	2.7e-4	1.9e-1	1.4e-2
32^3		14	7.8e-2	4.8e-3	8.9e-3	1.8e-3	1.3e-3	5.6e-5	4.7e-2	2.3e-3
8^3		8	3.4	3.2e-1	4.9	3.5	5.9e-2	4.2e-3	2.7e-1	2.6e-2
16^3	10	11	2.7e-1	2.3e-2	2.6e-1	1.2e-1	3.2e-3	2.2e-4	9.5e-2	5.6e-3
32^3		22	6.5e-2	4.0e-3	4.5e-2	1.0e-2	1.3e-3	4.7e-5	2.0e-2	8.2e-4
8^3		8	16	2.3	20	5.6	2.4e-1	3.0e-2	2.3e-1	2.2e-1
16^3	100	12	9.0	6.9e-1	23	4.8	3.0e-1	2.8e-2	4.8e-1	2.6e-2
32^3		23	2.2	1.4e-1	2.2	2.0e-1	4.4e-1	2.3e-2	1.2e-1	8.5e-3

Table 2: Synthetic problem with uniform grids: errors in the computed $\widehat{\boldsymbol{J}}$ and $\nabla\cdot\boldsymbol{A}$, and error indicators $\delta\boldsymbol{A}$ and $\delta\phi$. The value M is the number of iterations to convergence. Numbers in the left columns are measured in $\|\cdot\|_\infty$, in the right columns in $\|\cdot\|_2$. The number of cells, the mesh spacing h, and the number of unknown variables are provided at the top.

unit length, as well as discretization errors. Where a 2nd-order improvement is observed as h is decreased, we know that the discretization error dominates the finite-domain error.

The results of Table 2 are obtained using uniform grids. In particular, no special effort is made to cluster grid points in regions where the gradient of the conductivity is high; as such, the conductivity is essentially discontinuous on the scale of the resolution of the uniform grids. The fact that we are able to obtain accurate solutions in spite of the presence of discontinuities relates to our choice of formulation for the system of PDEs. The original field $\boldsymbol{E}$ has discontinuities in the normal direction across interfaces, but $\boldsymbol{A}$, ϕ, and $\widehat{\boldsymbol{J}}$ do not. Figure 5 illustrates this fact with a plot of a line of $\boldsymbol{A}$ and ϕ through the block of high conductivity. Similar results are obtained in [24] (which uses $\boldsymbol{A}$ in a magnetostatic problem) and in [20] (which uses $\boldsymbol{H}$ to handle discontinuities in σ and $\boldsymbol{E}$ to handle discontinuities in μ).

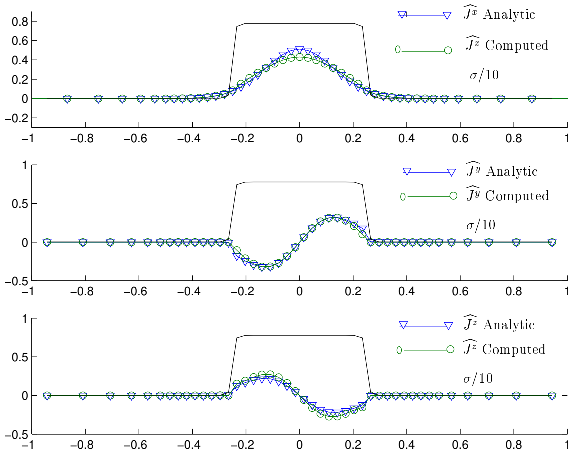

Figure 4: Synthetic problem: the real parts of computed current, $\widehat{\boldsymbol{J}}_c$, and the analytic current, $\widehat{\boldsymbol{J}}_a$, through a cross-section of the conductivity $\widehat{\sigma}$.

Finally, as a increases, the Krylov space iterative methods require more iterations to converge. Even so, the number of iterations needed to reduce the relative residual norm to 10^{-6} is very small compared with those reported in [25] (which uses standard Krylov-type methods and preconditioners).

For our second experiment, we compare the discretization (14) to the modification of the Yee discretization applied to the second-order system (2) (as described in Section 3.1). We contrast the number of BICGSTAB iterations and the corresponding number of operations (in gigaflops) needed to achieve a relative residual of 10^{-7} using each method. Since the modified Yee method does not produce a diagonally dominant system, we use an SSOR preconditioner with parameter value 1 for both methods, even though this does not show the discretization (14) at its best for low frequencies. The test problem is the synthetic model on uniform grids with $a = 100$. The results are summarized in Table 3. Table 3 demonstrates the rather substantial improvement that our method offers; at lower frequencies ω, this improvement is more pronounced.

Note that the convergence of the iterative solver for the Yee method is very slow because the source for this synthetic example is not divergence-free. The problem becomes more severe when the frequency ω is lower. Similar results were reported in [25] but not in [22], because the latter considers only magnetic sources which, unlike electric ones, are divergence-free.

ω	Grid	# of iterations $(\boldsymbol{A},\phi)$	$\boldsymbol{E}$	# of operations $(\boldsymbol{A},\phi)$	$\boldsymbol{E}$
	8^3	10	$> 10^5$	0.031	N/A
10^0	16^3	18	$> 10^5$	0.23	N/A
	32^3	32	$> 10^5$	14	N/A
	8^3	9	1542	0.029	2.1
10^6	16^3	26	2576	0.31	20
	32^3	42	5631	18	1200

Table 3: Comparison of $(\boldsymbol{A},\phi)$ and $\boldsymbol{E}$ formulations: iteration counts and computational work to solve the synthetic problem using BICGSTAB with SSOR preconditioning.

The grids in the first two experiments are uniform throughout the domain. Thus, for a third experiment, we solve the synthetic problem on non-uniform grids that widen exponentially towards the outer boundary. In one dimension, start with a uniform mesh on the interval $[-0.5, 0.5]$. At each end of the full interval, append a subinterval 1.3 times wider than the outermost subintervals. Repeat this process, padding the outside of the interval until the interval covers [-1,1]. Form a tensor-product grid in three dimensions from this non-uniform one-dimensional grid. This non-uniform grid allows us to avoid discretizing finely in regions where the solution does not vary much. We solve the synthetic problem on various exponentially widening non-uniform meshes and record the results in Table 4. The results in Table 4 indicate that the solution of (8b) is second-order accurate and that the number of iterations needed for convergence of the Krylov space methods is not affected significantly by the non-uniform grid.

The values for the discretization of $\nabla \cdot \boldsymbol{A}$ appearing in Tables 2 and 4 are nonzero, unlike in (17). This discrepancy is due to the finite-domain error which causes (3b) to be only approximately satisfied by the discretized PDE system, as well as the iteration error (ie. the Krylov iteration halts when the residual drops below a preset tolerance). Upon using the BCs (9) instead of (22), the values of $\|\nabla \cdot \boldsymbol{A}\|$ dropped significantly, depending now only on the iteration tolerance; however, for the reported values of L, a and h, the error in $\delta \widehat{\boldsymbol{J}}$ did not improve significantly.

We have also applied the method proposed in [1] to this synthetic model. For $a \leq 1$, the results are comparable in accuracy and iteration counts.

In that case, the method of [1] is somewhat preferable, because the cost per iteration is cheaper and the discretization does not involve a staggered grid which can simplify programming considerably. However, as a increases, the accuracy of the method in [1] deteriorates significantly, and the present method becomes superior. For $a = 100$, the method of [1] necessitates grid spacing that resolves the layers in $\widehat{\sigma}$ accurately before the solution error becomes adequately small. No such high resolution grid is necessary for the discretization (14).

5.2 A geophysical test problem

As a final test of our method, we compute the electric field at the surface of the earth due to an incident plane wave. This is a basic computation required in a magnetotelluric (MT) experiment [22]. The frequency is 10^3 Hz and we make the quasi-static assumption as in [1]. The conductivity structure is a block of high conductivity (10 S/m) in a low conductivity background (0.01 S/m). The BCs (22) are applied, with $\boldsymbol{g}(x, y, 1000) = (1, 0, 0)^T$ and $\boldsymbol{g}(x, y, -1000) = (0, 0, 0)^T$. Thus, there is no source current $\boldsymbol{J^s}$ and the fields are driven by the vertically incident plane wave. The goal is to find the electric field at the surface of the earth for the given frequency. The conductivity model is plotted in Figure 6.

We solve the forward modeling problem using an exponentially increasing grid as in the second experiment of Section 5.1. Contour plots of the three components of the electric field are presented in Figure 7. The solution is obtained in 22 iterations. From solving the problem on a large domain with various non-uniform grids, we observe that the number of iterations does not change significantly as long as $\omega\mu|\widehat{\sigma}|h \ll 1$, where h is the maximum grid spacing. This condition essentially ensures that the dominant differential terms in (19) remain dominant after discretization. In turn, the discrete system retains diagonal dominance as a consequence of the above bound.

The MT problem considered here does not admit a closed form solution. To verify our solution, we computed the solution again using another code [22],[4] which solves the first-order system of Maxwell's equations (1a,b) directly, with BCs imposed on $\boldsymbol{E}$. The discrepancies between the two results are less than 5%. The results deviate most on the edges and corners of the block of high conductivity. This is expected due to the differences in BCs

[4] available from `http://www.cg.emr.ca/mtnet`.

applied in the two codes, as well as errors due to discretization and interpolation.

When the frequency ω is increased, the diagonal blocks in (18) eventually lose their dominance. Correspondingly, the block ILU preconditioner loses efficiency. We have found an ILU-decomposition with a threshold applied to the entire system (18) to be a more robust preconditioner in such circumstances.

References

[1] D. Aruliah, U. Ascher, E. Haber, and D. Oldenburg. A method for the forward modelling of 3D electromagnetic quasi-static problems. *M3AS*, 1999. to appear.

[2] R. Barrett, M. Berry, T.F. Chan, J. Demmeland, J. Donato, J. Dongarra, V. Eijkhout, R. Pozo, C. Romine, and H. Van der Vorst. *Templates for the Solution of Linear Systems: Building Blocks for Iterative Methods*. SIAM, Philadelphia, 1994.

[3] R. Beck, P. Deuflhard, R. Hiptmair, R. Hoppe, and B. Wohlmuth. Adaptive multilevel methods for edge element discretizations of maxwell's equations. *Surveys Math. Indust.*, 1999. to appear.

[4] O. Bíró and K. Preis. On the use of the magnetic vector potential in the finite element analysis of three-dimensional eddy currents. *IEEE Transactions on Magnetics*, 25:3145–3159, 1989.

[5] A. Bossavit. *Computational electromagnetism. Variational formulation, complementarity, edge elements*. Academic Press, 1998.

[6] A. Bossavit and L. Kettunen. Yee-like schemes on staggered cellular grids: a synthesis between fit and fem approaches. *COMPUMAG*, 1999. Short contribution.

[7] A. Brandt and N. Dinar. Multigrid solution to elliptic flow problems. In *Numerical Methods for PDE's*, pages 53–147. Academic Press, New York, 1979.

[8] F. Brezzi and M. Fortin. *Mixed and Hybrid Finite Element Methods*. Springer-Verlag, New York, 1991.

[9] W.C. Chew. Electromagnetic theory on a lattice. *J. Appl. Phys.*, 75:4843–?, 1994.

[10] M. Clemens, R. Schuhmann, U. van Rienen, and T. Weiland. Modern Krylov subspace methods in electromagnetic field computation using the finite integration theory. *ACES J.*, 11:70–84, 1996.

[11] M. Clemens and T. Weiland. Numerical algorithms for the FDITD and FDFD simulation of slowly varying electromagnetic fields. *Int. J. Num. Modelling*, 1999. to appear.

[12] M.E. Everett and A. Schultz. Geomagnetic induction in a heterogenous sphere: Azimuthally symmetric test computations and the response of an undulating 660-km discontinuity. *J. Geophys. Res.*, 101:2765–2783, 1996.

[13] C.A.J. Fletcher. *Computational Techniques for Fluid Dynamics*, volume II. Springer-Verlag, 1988.

[14] V. Girault and P.A. Raviart. *Finite Element Methods for Navier-Stokes Equations*. Springer, Berlin-Heidelberg, 1986.

[15] P. M. Gresho and R. L. Sani. *Solutions of the incompressible Navier-Stokes equations*. Elsavir, 1998.

[16] E. Haber and U. Ascher. Fast finite volume modeling of 3d electromagnetic problems with highly discontinuous coefficients. *submitted*, 1999.

[17] R. Hiptmair. Multigrid method for maxwell's equations. *SIAM J. Numer. Anal*, 36:204–225, 1998.

[18] J.M. Hyman and M. Shashkov. Mimetic discretizations for Maxwell's equations. *J. Comp. Phys.*, 151:881–909, 1999.

[19] J.M. Hyman and M. Shashkov. The orthogonal decomposition theorems for mimetic finite difference methods. *SIAM J. Numer. Anal.*, 36:788–909, 1999.

[20] J. Jin. *The Finite Element Method in Electromagnetics*. John Wiley and Sons, 1993.

[21] D.J. LaBrecque. A scalar-vector potential solution for 3D EM finite-difference modeling. In M. Oristaglio and B. Spies, editors, *International Symposium on Three-Dimensional Electromagnetics*, pages 143–149. Schlumberger-Doll Research, 1995.

[22] R.L. Mackie, T.R. Madden, and P.E. Wannamaker. Three dimensional magnetotelluric modeling using difference equations - theory and comparison to integral equation solutions. *Geophysics*, 58:215–226, 1993. vol 2.

[23] C. Mattiussi. An analysis of finite volume, finite element, and finite difference methods using some concepts from algebraic topology. *Journal of Computational Physics*, 133:289–309, 1997.

[24] T. Nakata, N. Takahashi, and K. Fujiwara. Solutions of 3D eddy current problems by finite elements. *in: Finite element electromagnetics and design*, pages 36–72, 1995. Elsevier.

[25] G.A. Newman and D.L. Alumbaugh. Frequency-doman modelling of airborne electromagnetic responses using staggered finite differences. *Geophys. Prospecting*, 43:1021–1042, 1995.

[26] G.A. Newman and D.L. Alumbaugh. Three-dimensional magnetotelluric inversion using nonlinear conjugate gradients. *Geophysical journal international*, 140:410–418, 2000.

[27] Y. Saad. *Iterartive Methods for Sparse Linear Systems*. PWS Publishing Company, 1996.

[28] S. Selberherr. *Analysis and Simulation of Semiconductor Devices*. Wien: Springer-Verlag, 1984.

[29] A. Taflove. *Computational Electrodynamics: the Finite-Difference Time-Domain Method*. Artech House Publishers, 1995.

[30] Y. Tai. *Diadic Green Functions in Electromagnetics*. Elsevier, 1991.

[31] S. Turek. *Efficient Solvers For Incompressable Flow Problems*. New York: Macmillan, 1999.

[32] S.H. Ward and G.W. Hohmann. Electromagnetic theory for geophysical applications. *Electromagnetic Methods in Applied Geophysics*, 1:131–311, 1988. Soc. Expl. Geophys.

[33] T. Weiland. Time domain electromagnetic field computation with finite difference methods. *Int. J. Numer. Modelling*, 9:295–319, 1996.

[34] K. P. Whittall and D. W. Oldenburg. *Inversion of Magnetotelluric Data for a One Dimensional Conductivity*, volume 5. SEG monograph, 1992.

[35] K.S. Yee. Numerical solution of initial boundary value problems involving maxwell's equations in isotropic media. *IEEE Trans. on antennas and propagation*, 14:302–307, 1966.

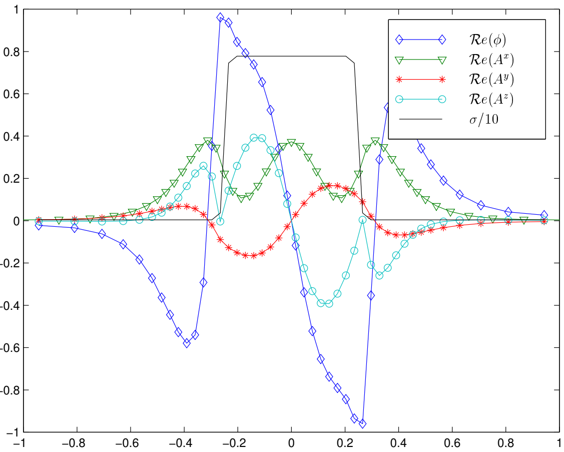

Figure 5: Synthetic problem: the real parts of computed solutions $\boldsymbol{A}$ and ϕ through a cross-section of conductivity $\widehat{\sigma}$.

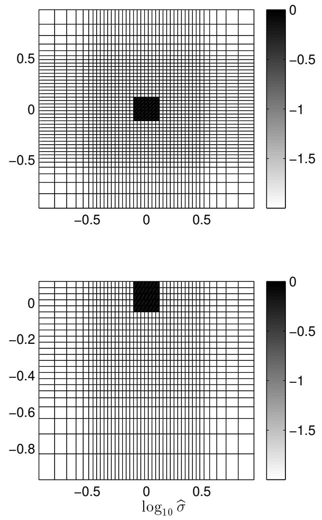

Figure 6: MT problem: a horizontal and a vertical cross-section of $\log_{10}\sigma$.

# cells	h^2	# variables
8^3	6.25e-2	4224
14^3	1.56e-2	22344
24^3	3.9e-3	111744
48^3	8.6e-4	889344

Grid	a	M	$\|\delta \boldsymbol{A}\|$		$\|\delta\phi\|$		$\|\nabla\cdot \boldsymbol{A}\|$		$\|\delta\widehat{\boldsymbol{J}}\|$	
8^3	0.5	4	2.2	2.6e-1	2.9e-1	1.0e-1	9.2e-2	8.6e-3	7.8e-1	9.2e-2
14^3		6	3.9e-1	3.9e-2	3.8e-2	4.6e-3	6.8e-3	6.3e-4	1.8e-1	1.7e-2
24^3		8	7.8e-2	7.2e-3	8.8e-3	2.3e-3	2.4e-3	1.6e-4	4.3e-2	3.5e-3
48^3		21	1.5e-2	1.7e-3	6.3e-3	1.8e-3	5.3e-4	4.1e-5	8.7e-3	8.5e-4
8^3	1.0	4	2.2	2.6e-1	3.3e-1	1.3e-1	4.8e-2	4.6e-3	7.5e-1	8.8e-2
14^3		6	3.9e-1	3.9e-2	4.1e-2	5.0e-3	3.6e-3	3.3e-4	1.9e-1	1.7e-2
24^3		8	7.8e-2	7.2e-3	8.9e-3	2.0e-3	1.3e-3	8.3e-5	4.4e-2	3.4e-3
48^3		23	1.5e-2	1.7e-3	3.8e-3	1.0e-3	2.8e-4	2.1e-5	8.7e-3	7.8e-4
8^3	10	10	3.4	3.2e-1	4.2	2.6	5.9e-2	4.2e-3	2.8e-1	2.6e-2
14^3		13	2.8e-1	2.9e-2	2.6e-1	1.2e-1	3.2e-3	2.6e-4	9.6e-2	6.9e-3
24^3		27	6.0e-2	5.8e-3	4.7e-2	1.3e-2	1.3e-3	7.2e-5	2.0e-2	1.2e-3
48^3		31	1.4e-2	1.7e-3	1.5e-2	3.9e-3	3.3e-4	1.8e-5	4.2e-3	2.8e-4
8^3	100	8	16	2.3	20	5.6	2.4e-1	3.0e-2	2.3e-1	2.2e-1
14^3		13	9.0	8.3e-1	23	5.6	3.0e-1	3.4e-2	4.8e-1	3.1e-2
24^3		21	2.2	2.1e-1	2.2	2.9e-1	4.4e-1	2.3e-2	1.e-1	8.4e-3
48^3		32	6.0e-1	5.7e-2	5.8e-1	9.1e-2	1.4e-1	1.0e-2	3.3e-2	2.3e-3

Table 4: Synthetic problem with non-uniform grids: errors in the computed $\widehat{\boldsymbol{J}}$ and $\nabla\cdot\boldsymbol{A}$, and error indicators $\delta\boldsymbol{A}$ and $\delta\phi$. The value M is the number of iterations to convergence. Numbers in the left columns are measured in $\|\cdot\|_\infty$, in the right columns in $\|\cdot\|_2$. The number of cells, the mesh spacing h in the central region $[-.5,.5]$, and the number of unknown variables are provided at the top.

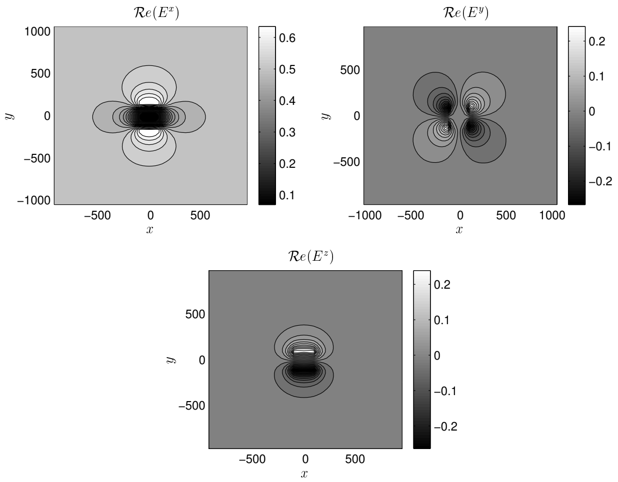

Figure 7: MT problem: contour plots of the computed solution $\mathcal{R}e(\boldsymbol{E})$ at the air-earth interface ($\boldsymbol{E}$ is scaled so that $\boldsymbol{E}(x, y, z = 2000) = (1, 0, 0)^T$).